



Optimizing electrocatalytic oxygen reduction by adjacent C-O-C structure-driven charge separation on FeN₄ active sites

Bin Zhao^{a,e,1}, Dongping Xue^{a,e,1}, Pengfei Yuan^c, Wenfu Yan^d, Jiangwei Zhang^f, Shichun Mu^b, Jia-Nan Zhang^{a,e,*}

^a College of Materials Science and Engineering, Zhengzhou University, Zhengzhou 450001, PR China

^b State Key Laboratory of Advanced Technology for Materials Synthesis and Processing Wuhan University of Technology, Wuhan 430070, PR China

^c International Joint Research Laboratory for Quantum Functional Materials of Henan Province, and School of Physics and Microelectronics, Zhengzhou University, Zhengzhou 450001, PR China

^d State Key Laboratory of Inorganic Synthesis and Preparative Chemistry, and College of Chemistry, Jilin University, Changchun 130012, PR China

^e Key Laboratory of Advanced Energy Catalytic and Functional Material Preparation of Zhengzhou City, Zhengzhou 450012, PR China

^f State Key Laboratory of Catalysis & Gold Catalysis Research Center, Dalian Institute of Chemical Physics, Chinese Academy of Sciences (CAS), Dalian 116023, PR China

ARTICLE INFO

Keywords:

Density functional theory

Oxygen-doping

Fe single-atom catalyst

Oxygen reduction reaction

Zn-air battery

ABSTRACT

The preparation of single atom (SA) Fe-N-C catalysts always results in the formation of an oxygen(O)-containing moieties. The effect of the oxygen-containing part on the oxygen reduction reaction (ORR) conducted with Fe-N-C is often overlooked, and the mechanism of the contribution of the oxygen-doping structure remains ambiguous. Therefore, guided by density functional theory (DFT) calculations, the adjacent C-O-C structure promotes the charge separation of the active center of FeN₄ and reduces the adsorption of O-containing intermediates, which significantly increase the ORR kinetics. To experimentally verify such principle, we design the SA FeN₄ catalysts (FeN₄-700/900) incorporating in carbon substrates derived from O-rich biomass. The FeN₄-700/900 catalyst displays enhanced ORR activity under acidic (0.78 V) and alkaline (0.904 V) conditions over FeN₄-700/700 and FeN₄-900/900 catalysts, while exhibiting excellent Zn-air battery performance. This work opens an avenue to explore the modulation of the active site and the practical application of Fe-N-C catalysts.

1. Introduction

Oxygen reduction reaction (ORR) as the vital cathode reaction for fuel cells and metal-air batteries is currently highly dependent on Pt-based catalysts, whereas the exorbitant cost, poor durability, and methanol tolerance greatly hamper their massive applications [1–3]. Considering the great challenge of seeking for non-precious metal carbon-based catalysts, N-coordinated single-atomic metal-based carbon (SA M-N-C) catalysts have attracted extensive attention for the high atom utilization, uniform active sites, tunable electronic structure, and high catalytic activity [4–6]. Among them, SA Fe-N-C catalysts are regarded to be the most promising alternative to precious metal-based catalysts because of the electron-absorbing property of carbon, the performance of the Fe-N-C catalysts is greatly superior to that of other non-precious metal catalysts [7,8]. The Fe-N-C catalyst can be further

optimized by a strategy to control the atomic configuration around the SA FeN₄ site, but it still needs to be further elucidated [9,10].

Regarding the practical preparation of Fe-N-C catalyst, residual O-containing moieties (e.g., C-O-C, edged C-OH, and C=O) are inevitable even at high temperature annealing under inert atmosphere, due to the difficulties of complete removal of adsorbed oxygen or the strong binding of oxygen functional groups on the raw material [11–13]. Therefore, it actually becomes a controversial topic to clarify the character of the catalytic site in Fe-N-C with the additional O-containing active site. Jung et al. had reported the atomic-level tuning of Co-N-C catalyst by C-O-C moiety for high selectivity of H₂O₂ production [14]. Xiong et al. used oxygen-containing functional groups to activate poorly performing main group metal elements, resulting in high ORR activity of Sb-N₄ [15]. However, the uncontrollable types of O-containing active site make it the complexity of reaction mechanisms on the surface of

* Corresponding author at: College of Materials Science and Engineering, Zhengzhou University, Zhengzhou 450001, PR China.

E-mail address: zjn@zzu.edu.cn (J.-N. Zhang).

¹ The corresponding author's contribution equally.

Fe-N-C electrocatalysts causes incredible challenges for the rational design.

Biomass materials contain a large number of O-rich functional groups that can be converted by pyrolysis into carbon substrates with different oxygen contents and structures [16–18]. The low cost and renewable advantages also render biomass carbon materials to be considered as promising carbon materials for solving large-scale and economical preparation of non-precious metal catalysts [19]. In addition, biomass-derived carbon has excellent macro-, meso-, and micro-structures, which favors the ORR mass transfer process [20–22]. Therefore, the abundant O-doping and the unique hierarchical porous structure make the biomass carbon substrate offer the possibility to probe the effect of O-doping on Fe-N-C catalysts [23].

Herein, we propose a strategy to regulate the electronic microenvironment of the Fe-N₄ active center by optimizing the O-doping position. Theoretically, density functional theory (DFT) calculations indicate that O-doping promotes charge separation in the Fe-N₄ active center, and the downward shift of the *d*-band center weakens the adsorption of O-containing intermediates. Notably, the short-range C-O-C structure further promotes charge separation of FeN₄ configurations and significantly lowers the reaction energy barrier, resulting in the better intrinsic activity of the Fe-N-C catalysts. Experimentally, Fe single atoms are anchored on the carbon substrates derived by the oxygen-rich biomass (chestnut inner shells). As expected, along with the controlled carbonized process, the activity-dependent O-doping configurations forms surround the FeN₄ center for elucidating the nature of catalytic centers (FeN₄-700/900). Take the advantages of unique structures, as-prepared FeN₄-700/900 catalyst exhibits excellent ORR activity under acidic and alkaline conditions, which significantly superior to N, O co-coordinated Fe SACs (FeN₄-700/700), and standard FeN₄-900/900 catalysts. Meanwhile, FeN₄-700/900 catalyst displays outstanding Zn-air battery performance. This work clarifies the mechanism of the role of O-doping for Fe-N-C catalysts, and also opens a pathway to explore the modulation of the active site and the practical application of Fe-N-C materials.

2. Experimental

2.1. Synthesis of carbon substrates with different degree of O-doping

The oxidized carbon substrate was synthesized via an etching-activation approach. Typically, the chestnut inner shells were first cleaned with deionized water and dried at 60 °C, and then was mixed with NaOH and ground for 30 min. The mixture was heated at 700 °C for 2 h at a rate of 5 °C/min under Ar atmosphere. The obtained powder was washed with 0.5 M H₂SO₄ at 80 °C for 4 h, and centrifuged with deionized water and ethanol until the filter was neutral. Then the acid-washed sample was dried at 60 °C in a vacuum oven for 12 h to obtain carbon substrates. Carbon substrates with different O-doping degree were pretreated at different temperatures (700 or 900 °C), with 700 °C labeled as O-rich carbon substrate (C_{OR}) and 900 °C labeled as O-deficient carbon substrate (C_{OD}).

2.2. Synthesis of FeN₄-700/700, FeN₄-700/900 and FeN₄-900/900

Typically, a mixture of 50 mg of the carbon substrates (oxidized carbon), 250 mg of melamine, and 56 mg of Fe(NO₃)₃·9H₂O were mixed in 50 mL of deionized water and stirred at 80 °C for 4 h. After centrifugation, the sample was dried at 60 °C in a vacuum oven for 12 h. The powder obtained was carbonized in a tubular carbonization furnace at 900 °C for 2 h by heating at 5 °C/min in Ar atmosphere. It was subsequently acid-treated at 80 °C for 4 h to remove the metal particles and labeled as FeN₄-700/900. As control samples, FeN₄-700/700 was obtained by pyrolysis of metal-loaded C_{OR} at 700 °C and FeN₄-900/900 was obtained by pyrolysis of metal-loaded C_{OD} at 900 °C. The three materials that used the same synthesis method but without the adsorbed metal ions are named NC-700/700, NC-700/900 and NC-900/900

accordingly.

2.3. Characterizations

This research mainly involves the following characterization methods to analyze the physical and chemical properties of materials. The crystal phases present in each sample were identified using powder X-ray diffraction (XRD) patterns recorded by an X'Pert PRO X-ray Diffractometer using copper K α radiation ($\lambda = 1.5406 \text{ \AA}$) at 40 kV, 45 mA. The structure of the samples was characterized by a transmission electron microscope (TEM, JEM 2100 F) and a field-emission scanning electron microscope (FE-SEM, JEORJSM-6700 F). The X-ray photoelectron spectroscopy (XPS) measurements were performed with an Thermo Scientific K-Alpha spectrometer. The Raman measurements were taken at 532 nm on a Renishaw Microscope System RM2000. N₂ adsorption/desorption curves were obtained by BET measurements using a Micromeritics ASAP 2020 surface area analyzer. O K-edge X-ray absorption spectra were collected on the soft X-ray beamline at National Synchrotron Radiation Laboratory (NSRL) Hefei, China. The X-ray absorption fine structure spectra (Fe K-edge) were collected at 1W1B station in Beijing Synchrotron Radiation Facility (BSRF). All spectra were collected in ambient conditions. Use Athena software to process XAS data, including background subtraction, normalization of edge skipping, and Fourier transform of k^2 -weighted $\chi(k)$ data. To obtain the quantitative structural parameters around central atoms, least-squares curve parameter fitting was performed using the ARTEMIS module of IFEFFIT software packages [24–26].

2.4. Electrocatalytic measurements

All electrochemical measurements of the electrocatalytic activity to ORR were performed using a CHI Electrochemical Station (Model 760E) in a conventional three-electrode cell at room temperature. A glassy carbon rotating disk electrode (GC-RDE) was used as the working electrode. A platinum wire was used as the counter electrode, Ag/AgCl as the reference electrode, and 0.1 M KOH as the alkali electrolytes. All potentials used in this work have been converted to the RHE scale. The catalyst inks were prepared by mixing 5 mg of the catalyst in 0.5 mL of a solution containing 335 μL of isopropyl alcohol, 145 μL of deionized water and 20 μL of a 5% Nafion solution, followed by ultrasonication for 30 min to form homogeneous inks that were drop-cast onto the GC-RDE and air-dried. The catalyst loading was 0.1 mg cm^{-2} .

All electrochemical measurements were carried out at room temperature (26 °C) using a rotating disk electrode (RDE, Pine Instrument). The linear sweep voltammetry (LSV) of the catalyst in an alkaline electrolyte was measured in an O₂-saturated KOH (0.1 M) water solution with rotation speeds from 400 to 2500 rpm. The Tafel slopes were calculated according to the Tafel equation $\eta = b \log(j/j_0)$ based on the LSV curves, where η is the overpotential, b is the Tafel slope, j is the current density, and j_0 is the current exchange density. Stability was examined by current-time chronoamperometry.

Durability tests were performed by applying potential cycling at a sweep rate of 100 mV s^{-1} for 10,000 cycles. For ORR at a RDE, the electron transfer number (n) and kinetic current density (J_K) were calculated from the Koutecky-Levich equation:

$$\frac{1}{J} = \frac{1}{J_L} + \frac{1}{J_K} = \frac{1}{B\omega^{0.5}} + \frac{1}{J_K} \quad (1)$$

$$B = 0.62nFC_0(D_0)^{2/3}\nu^{-1/6} \quad (2)$$

$$J_K = nFkC_0 \quad (3)$$

where J is the measured current density and is the electrode rotation rate (rad s^{-1}). B is determined from the slope of the Koutecky-Levich (K-L) plot based on the Levich Eq. (2). J_L and J_K are the diffusion- and kinetic-

limited current densities, n is the number of electrons transferred, F is the Faraday constant ($F = 96,485 \text{ C mol}^{-1}$), C_0 is the O_2 concentration in the electrolyte ($C_0 = 1.26 \times 10^{-6} \text{ mol cm}^{-3}$), D_0 is the diffusion coefficient of O_2 ($D_0 = 1.93 \times 10^{-5} \text{ cm}^2 \text{ s}^{-1}$), and v is the kinetic viscosity ($v = 0.01009 \text{ cm}^2 \text{ s}^{-1}$). The constant 0.62 is used when the rotation speed is expressed in rad s^{-1} .

For the RRDE measurements, catalyst inks and electrodes were prepared by the same method as for RDE. The disk electrode was scanned at a rate of 5 mV s^{-1} , and the ring potential was constant at 0.336 V in 0.1 M KOH (vs. Ag/AgCl). The hydrogen peroxide yield ($\text{H}_2\text{O}_2\%$) and transfer number (n) were determined from the following equations [27]:

$$\text{H}_2\text{O}_2(\%) = 200 \times \frac{I_R/N}{I_D + I_R/N} \quad (4)$$

$$n = 4 \times \frac{I_D}{I_D + I_R/N} \quad (5)$$

where I_d is the disk current, I_r is the ring current, and N is the current

collection efficiency of the Pt ring. N was determined to be 0.40.

2.5. Zinc-air battery tests

All Zn-air batteries were evaluated under ambient conditions. The catalyst ink was prepared by dispersing 5 mg catalyst in $480 \mu\text{L}$ of DI water/isopropyl alcohol ($v/v \sim 3:7$) with 5 wt\% Nafion as a binder. The mixture was sonicated for 30 min to obtain a uniform suspension. For the Zn-air battery test, the air electrode was prepared by uniformly coating the as-prepared catalyst ink onto carbon paper and then drying it at 80°C for 2 h . The mass loading was 0.2 mg cm^{-2} unless otherwise noted. A Zn plate was used as the anode, and the catalyst loaded on carbon paper was used as the cathode. Both electrodes were assembled into a home-made Zn-air battery and a 6 M KOH aqueous solution with $0.02 \text{ M Zn(NO}_3)_2$ (dissolved in KOH to form zincate, Zn(OH)_4^{2-}) was used as the electrolyte to ensure reversible zinc electrochemical reactions at the anode. The specific capacity and energy density were calculated from the galvanostatic discharge results normalized to the mass of

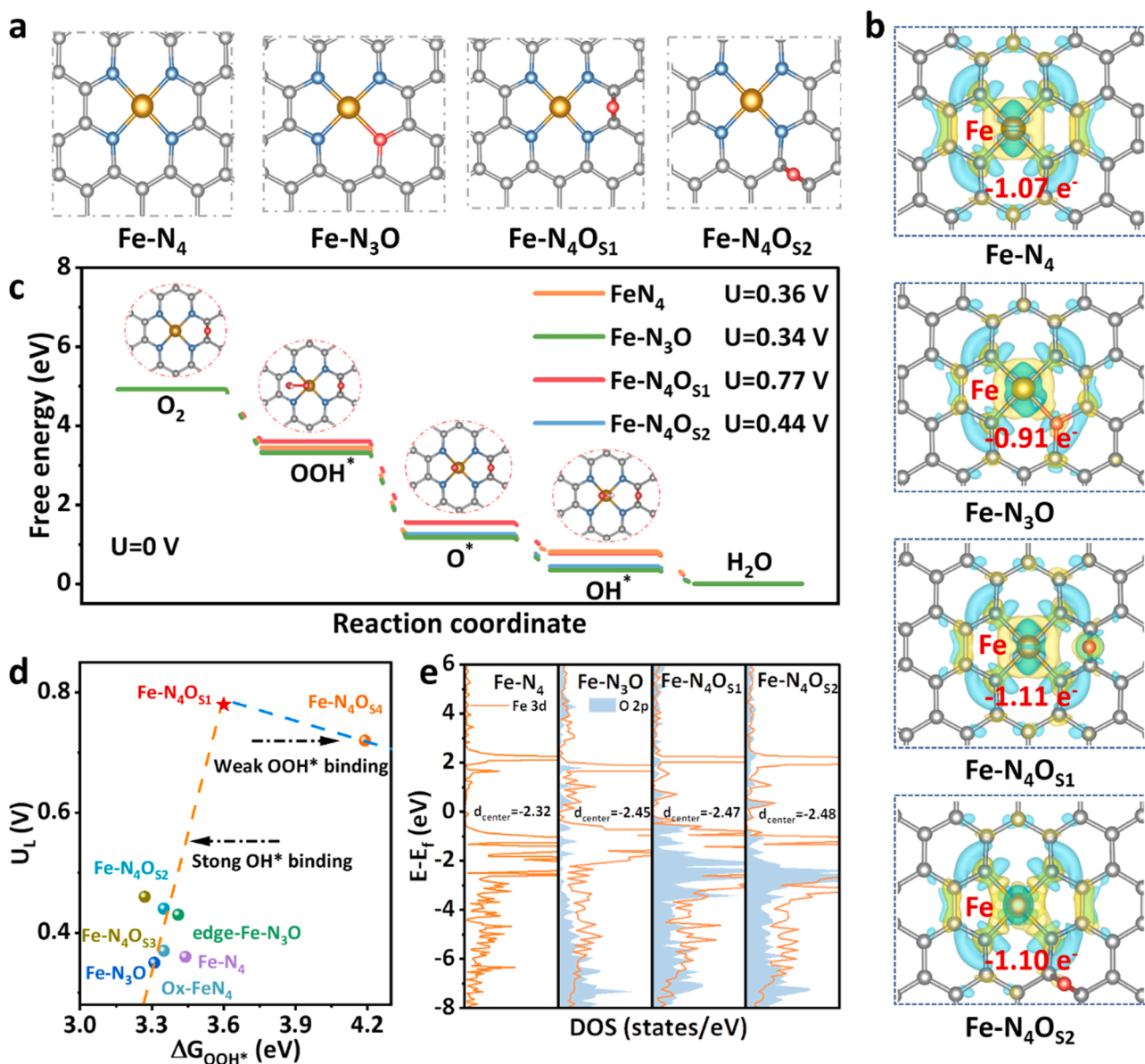


Fig. 1. Theoretical predictions of Fe-N-C catalysts. (a) Optimal computational model of Fe-N₄ molecules with different O-doping. (b) The calculated charge density distribution in Fe-N₄, Fe-N₃O, Fe-N₄O_{S1} and Fe-N₄O_{S2}. (c) ORR free energy of different models at the ultimate voltage. (d) Calculated catalytic activity volcanoes for the production of H₂O via the ORR. The U_L is plotted as a function of ΔG_{OOH^*} . (e) The DOS of Fe and O in Fe-N₄, Fe-N₃O, Fe-N₄O_{S1} and Fe-N₄O_{S2}.

consumed Zn. The mass of consumed Zn was determined by the difference between the fresh Zn and resultant anode after discharging.

3. Results and discussion

3.1. Mechanistic analysis

To reveal the mechanism of O-doping, we performed periodic DFT calculations to identify active center along with different O-doping structures on the Fe-N₄ active site. There are three possible doping positions for O: i) O is directly coordinated with the metal active center, forming N, O-M. ii) Present around Fe-N₄ in the form of oxygen-containing groups. iii) Present in Fe-N-C in the form of oxidized N. Previous studies have demonstrated that the effect of oxidized N on ORR is essentially negligible [28]. Computational models established are shown in Fig. 1a and S1, which focus on the involvement of O in Fe coordination and the presence of O around FeN₄ with C-O-C structure, while the standard Fe-N₄ structure is also studied as a model for comparison. Firstly, the charge density difference and Bader charge of FeN₃O, FeN₄O_{S1}, FeN₄O_{S2}, and Fe-N₄ structures were comparatively calculated to reveal the effect of O doping on the electronic structure of the active center, as shown in Fig. 1b. The yellow color indicates the accumulation of charge and the green color indicates the depletion of charge. Compared with standard Fe-N₄, O-doping modulates the electronic structure of the active center, resulting in electron redistribution in Fe-N₄. When O is doped in the FeN₃O structure, it results in the transfer of electrons from O to Fe, which reduces the charge separation on Fe (the valence state of Fe decreases). When O is doped in the form of C-O-C, there are two structures: adjacent (FeN₄O_{S1}) and distant (FeN₄O_{S2}), since C-O-C is an electron withdrawing group, the charge separation on Fe is enhanced (the valence state of Fe is increased), and the positive charge density is accumulated on the active center Fe. Further Bader charge analysis not only verified the above results, but also demonstrated that Fe in the FeN₄O_{S1} structure loses more electrons than the FeN₄O_{S2} structure, indicating that the doping of the adjacent C-O-C structure makes the FeN₄ center have a stronger charge separation effect.

The corresponding Gibbs reaction free energy of the four structural models are shown in Fig. 1c, when the electrode potential is 0 V, each step of the ORR free energy diagram for all models is thermodynamically downward, indicating that all processes are exothermic and can proceed completely spontaneously. The optimized structures of the four models for the adsorbed oxygen intermediates are shown in Fig. S2-S7. The calculation of the corresponding ORR free energy at 1.23 V appears as a thermodynamically upward step. The third electron transfer step ($O^* + 2H^+ + 2e^- + H_2O \rightarrow OH^* + H^+ + e^- + H_2O$) is the rate-determining step (RDS) for the Fe-N₄ model because of the highest energy barrier ($\Delta G=0.87$ V) [29]. The RDS after O-doping becomes $OH^* + H^+ + e^- + H_2O \rightarrow * + 2H_2O$, corresponding to ΔG for FeN₃O (0.883 V), FeN₄O_{S1} (0.46 V) and FeN₄O_{S2} (0.793 V), respectively. The O-doping changes the RDS while decreasing the reaction energy barrier, where FeN₄O_{S1} exhibits the lowest overpotential and significantly increases the thermodynamic limit potential (0.77 V) (Fig. 1d). Previous studies have shown that the poor catalytic activity of Fe-N₄ is mainly due to the strong adsorption of oxygen intermediates [30]. According to the d-band center theory [31], the density of states (DOS) analysis show that the doping of the adjacent C-O-C makes the d-band center of the FeN₄ structure move down, weakening the adsorption of oxygen intermediates and thus promoting the ORR, and also verifies the excellent ORR activity of FeN₄O_{S1} structure (Fig. 1e). All mentioned above demonstrate that the structure of C-O-C adjacent to FeN₄ changes the RDS of ORR, significantly reduces the reaction overpotential, weakens the adsorption to oxygen intermediates and thus improves the intrinsic activity of ORR.

3.2. Catalyst synthesis and characterization

To experimentally verify the effect of O-doping in Fe-N₄ for ORR, we tried to control the O content and O species structure by careful design of pyrolysis processes of both biomass-derived carbon support and Fe-N-C catalysts. As shown in Fig. 2a, the chestnut inner shell is treated with NaOH at 700 °C to produce an oxygen-rich carbon substrate (C_{OR}), and similarly at 900 °C to obtain a less oxygenated carbon substrate (C_{OD}). After adsorption of Fe on C_{OR}, the Fe-N-C materials synthesized at 700 °C and 900 °C are denoted as FeN₄-700/700 and FeN₄-700/900, respectively. For comparison, the FeN₄-900/900 catalyst is also prepared at 900 °C on C_{OD}. Fourier transform infrared spectroscopy (FTIR) shows that the intensity of the C-O-C peaks gradually decreased with increasing temperature (Fig. 2b), indicating that the proportion of the C-O-C structure in Fe-N-C gradually decreased with the increase of temperature. The O1s spectra are assigned to Fe-O and C-O-C bonds at 531 eV and 532.2 eV, and to C-O phenolic as well as chemisorbed water around 533.5 eV (Fig. 2c and Table S1). It shows a sharp decrease in the Fe-O bond from 42.7% to 6.2% and an increase in the C-O-C content, further confirming the change in O species structure indicating that the O-doping form changes from direct coordination with the active center to the C-O-C adjacent to FeN₄. As shown in Fig. 2d, the oxygen contents of C_{OR}, FeN₄-700/700, FeN₄-700/900, and FeN₄-900/900 are 7.8, 5.6, 4.3, and 3.1 at%, while the ratios of C-O-C and Fe-O in FeN₄-700/900 has a significant increase, strongly suggesting that the O content and structure are correlated with the annealing temperature (T). The soft O K-edge XANES can explore further information about oxygen functional groups. As shown in Fig. S8a, C_{OR} has the stronger O K-edge signal compared to C_{OD}, which is attributed to the modulation of oxygen content in the substrate by different pyrolysis temperatures. In Fig. S8b, FeN₄-700/900 exhibits more intense peaks at 535.9 and 542.2 eV, which are mainly assigned to C-O bonds in π^* and σ^* states (e.g., C-O-C). Previous studies have shown that the C=O (π^*) located at 533.2 eV is characteristic of peaks associated with carbonyl-related groups [32]. To investigate the effect of metals for oxygen functional groups, three corresponding NC materials (NC-700/700, NC-700/900, NC-900/900) without adsorbed metals are added to the experiment. As shown in Fig. S8c and Table S2, the O1s spectrum is assigned to C=O and C-O-C bonds at 531 eV and 532.3 eV, and C-OH at around 533.5 eV as well as chemisorbed water. In comparison with the corresponding FeN₄-700/700, FeN₄-700/900 and FeN₄-900/900 catalysts, the introduction of Fe atoms has a limited effect on the oxygen content but the C=O bond changes to Fe-O bond. As the temperature increases, the form of O atoms present changes, the content of C=O bonds decreases and the C-O-C content increases, which is consistent with Fe-N-C. In summary, FTIR, XPS, and NEXAFS comprehensive analyses can demonstrate that the content and configuration of O-doping can be carefully designed to reasonably control the pyrolysis temperature of the carbon substrate and the final catalyst.

As shown in Fig. 2e and S9b-c, FeN₄-700/900 has the same nano-sheet structure as the carbon substrates, indicating that the structure is not changed after loading of metal. To further explore the distribution of Fe atoms, we perform aberration-corrected high-angle annular dark-field scanning TEM (AC HAADF-STEM) measurements on FeN₄-700/900. As shown in Fig. 2f and 2g, the sample can be observed that Fe atoms are atomically scattered on the carbon substrate and the red circles mark Fe single atoms. Additionally, the energy dispersive spectrum (EDS) elemental mapping images indicate that C, N, O, and Fe elements are evenly distributed in the FeN₄-700/900 catalysts (Fig. 2h). The X-ray diffraction (XRD) patterns (Fig. S10a) of the FeN₄-700/900 and C_{OR} exhibit broad peak at 24.7°, which has probably been attributed to the (002) plane of graphitic carbon. There are no characteristic peaks detected in the XRD images of FeN₄-700/900 associated with Fe particles. Inductively coupled plasma (ICP) measurements identified the Fe content as ~0.65 wt%.

Raman spectroscopy is employed to examine the D-band to G-band

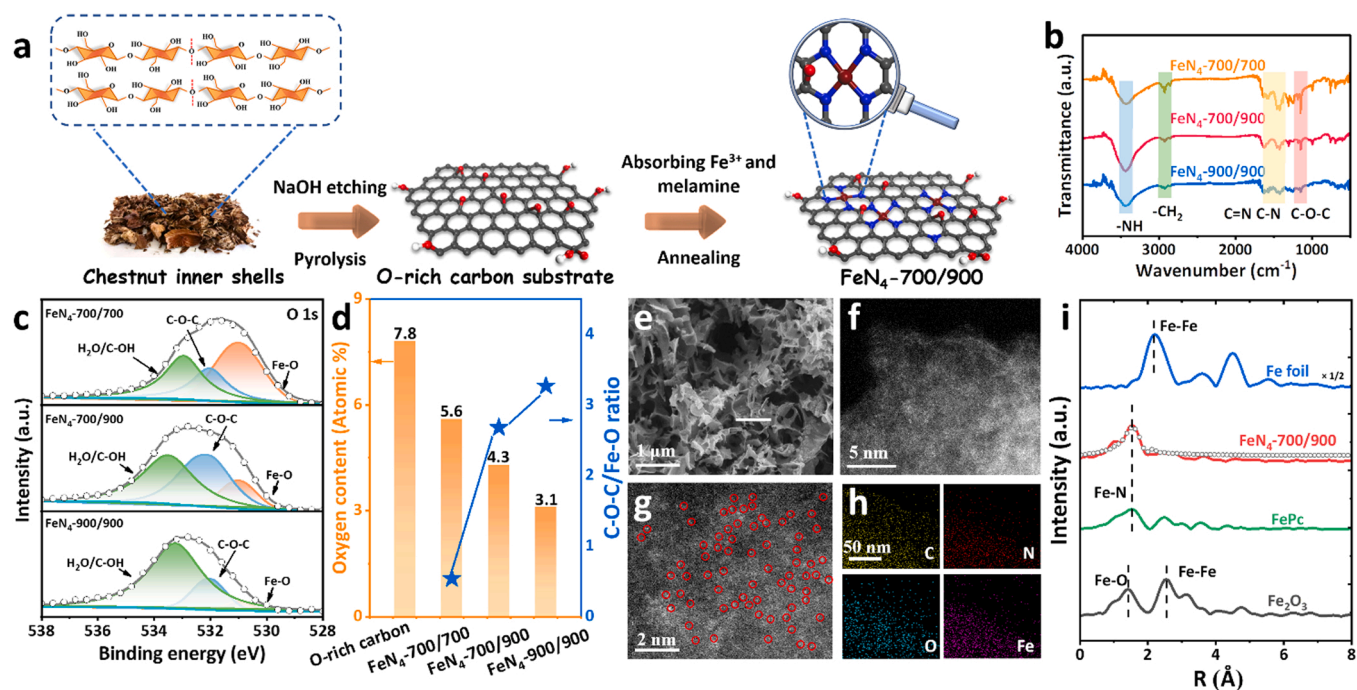


Fig. 2. Synthetic procedure and structural characterization of Fe-N-C catalysts. (a) Synthetic procedure of Fe-N-C catalyst. (b) FTIR spectra of FeN₄-700/700, FeN₄-700/900 and FeN₄-900/900. (c) O 1s XPS spectra for FeN₄-700/700, FeN₄-700/900 and FeN₄-900/900, respectively. (d) Oxygen content and C-O-C/Fe-O structural ratios of O-rich carbon (C_{OR}), FeN₄-700/700, FeN₄-700/900 and FeN₄-900/900. (e) SEM image of the FeN₄-700/900. (f, g) Atomic-resolution HAADF-STEM images of the FeN₄-700/900. Single Fe atoms highlighted by red circles. (h) HAADF-STEM images, corresponding element maps showing the distribution of C (yellow), N (red), O (blue), and Fe (purple). (i) Fourier-transformed k^2 -weighted EXAFS spectra for FeN₄-700/900 and reference materials.

intensity ratio (I_D/I_G) in samples, which is sensitive to the degree of graphitization of the carbon-based catalysts [33]. The results show that the I_D/I_G ratio of FeN₄-700/900 is reduced compared to C_{OR}, indicating that the degree of graphitization of FeN₄-700/900 increases significantly with the addition of Fe (Fig. S11a and S11b). With the annealing temperature increasing, the calculated I_D/I_G ranges from 1.34 to 1.19 for the Fe-N-C samples, implying the improvement in graphitization with the pyrolysis temperature, increasing the conductivity of the catalyst. As shown in Fig. S11c, the N₂ adsorption/desorption isotherm of FeN₄-700/900 and C_{OR} are typical type IV isotherm and hysteresis loop [34,35]. The closure of the hysteresis loop at $P/P_0 = 0.5$ indicates the microporous and mesoporous structures. It can be seen from the pore size distribution curve that FeN₄-700/900 and C_{OR} contained abundant microporous and mesoporous structures (Fig. S11d), which is beneficial to the anchoring of active sites and the mass transfer in the ORR process. The C 1s XPS spectrum shows three peaks at 284.8, 285.9, and 287.1 eV, which can be attributed to C-C, C-O-C, and C=O groups, respectively (Fig. S13a) [36]. The N 1s spectrum (Fig. S13b) can be well deconvoluted into five peaks located at 403, 401.3, 400.3, 399.4, and 398.5 eV, corresponding to oxidized N, graphitic N, pyrrolic N, Fe-N and pyridinic N, respectively (Table S3) [37]. Previous studies have shown that pyridine N is essential in the formation of Fe-N-C active sites because of its better thermodynamic stability during formation while favoring improved ORR performance [38,39]. The large occupation of C-O-C and pyridine N in FeN₄-700/900 is favorable to improve the ORR activity. All the above characterizations indicate that the strategy of temperature-controlled O-doping is reasonable.

X-ray absorption near-edge structure (XANES) is further performed to elucidate the structure of Fe-N-C at the atomic level [40]. As shown in Fig. S14a, the XANES curve of FeN₄-700/900 is located at the near-edge absorption energy between FePc and Fe₂O₃, indicating that the Fe is positively charged and the valence state of Fe is between Fe^{II} and Fe^{III}. The Fourier-transformed EXAFS (FT-EXAFS) can reveal more information of the atomic structure [41]. In the range of k values from 0 to

12 \AA^{-1} and weighted by 2 Fourier transform EXAFS, FeN₄-700/900 has no obvious metal interaction causing oscillatory signals in the high k region, indicating that a single-atom catalyst is synthesized (Figs. S14b and S14c). As shown in Fig. 2i, FeN₄-700/900 has one peak at $\sim 1.55 \text{ \AA}$, which is in the same position as the Fe-N coordination in FePc, indicating that the active sites of FeN₄-700/900 are similar to that of FePc. The Fe-Fe peak in Fe foil is located at about 2.2 \AA , which is not detected in FeN₄-700/900. This further shows that FeN₄-700/900 does not form Fe nanoparticles, and Fe sites existed in the form of atomic dispersion, which are consistent with the above-mentioned TEM and XRD results. A least-squares EXAFS fit is also performed to obtain the quantitative chemical configuration of the iron atoms [42]. The fitting result depicts that the isolated Fe atom is coordinated by four N atoms with an average bond length of 1.99 \AA (Table S3). In order to show more clearly the atomic dispersion throughout FeN₄-700/900, a wavelet transform (WT) is conducted on the Fe K-edge EXAFS oscillations as its powerful resolution in both k and R space [43]. The WT contour plots of Fe foil, FePc, and Fe₂O₃ (Fig. S15) inform that the intensity maxima at 3.5 and 7 \AA^{-1} are associated with the Fe-N and Fe-Fe contributions. Impressively, the WT contour plot of FeN₄-700/900 displays only one intensity maximum at 3.5 \AA^{-1} , which can be ascribed to the Fe-N coordination.

3.3. Catalytic performance

The catalytic activity of the designed Fe-N-C for ORR is measured mainly in alkaline conditions [44]. As shown in Fig. S16a and S16b, the cyclic voltammetry (CV) curves and linear sweep voltammetry (LSV) curves are obtained by rotating disk electrode (RDE). FeN₄-700/900 exhibits excellent ORR performance at 0.1 M HClO_4 (Fig. 3a). The $E_{1/2}$ of FeN₄-700/900 (0.78 V) approaches the $E_{1/2}$ of commercial Pt/C (0.82 V) better than FeN₄-900/900 (0.76 V) and FeN₄-700/700 (0.72 V). As shown in Fig. 3b, FeN₄-700/900 shows the half-wave potential ($E_{1/2}$) of about 0.904 V (vs. RHE) at 0.1 M KOH , which is more positive compared to FeN₄-700/700 (0.823 V), FeN₄-900/900

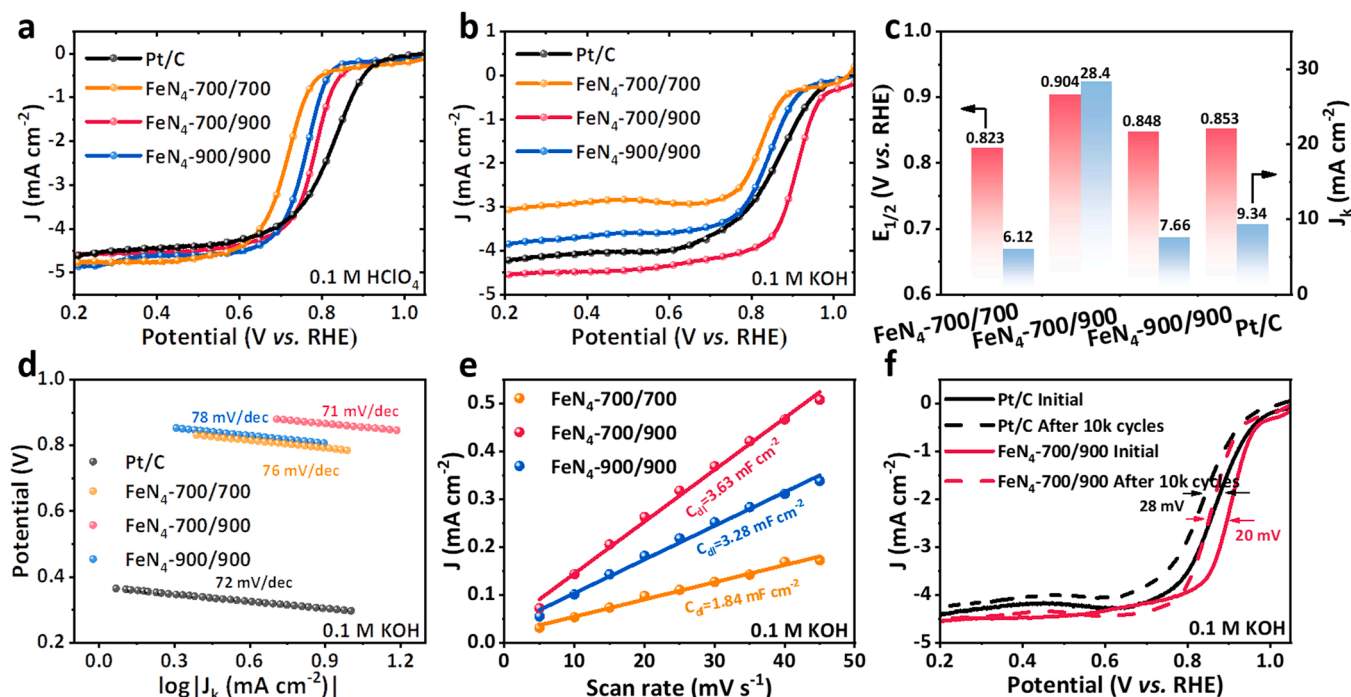


Fig. 3. Evaluation of ORR performance of different catalysts. (a) LSV curves for FeN₄-700/700, FeN₄-700/900, FeN₄-900/900 and Pt/C in O₂-saturated 0.1 M HClO₄ with a rotating rate of 900 rpm. (b) LSV curves for FeN₄-700/700, FeN₄-700/900, FeN₄-900/900 and Pt/C in O₂-saturated 0.1 M KOH with a rotating rate of 900 rpm. (c) Comparison of $E_{1/2}$ and J_k at 0.8 V for various electrocatalysts in O₂-saturated 0.1 M KOH. (d) Tafel plots. (e) Dependence of current densities as a function of scan rates at 1.16 V vs. RHE. (f) ORR polarization curves of FeN₄-700/900 and Pt/C in O₂-saturated 0.1 M KOH before and after 10 000 circles of ADT at a scan rate of 100 mV s⁻¹ at 0.6–1.0 V (vs. RHE).

(0.848 V), and 51 mV more positive to Pt/C (0.853 V). The kinetic current densities of the catalysts at 0.8 V (vs. RHE) are shown in Fig. 3c. FeN₄-700/900 exhibits a kinetic current density of 28.4 mA cm⁻², which is vastly enhanced compared with FeN₄-700/700 (6.12 mA cm⁻²), FeN₄-900/900 (7.66 mA cm⁻²) and Pt/C (9.34 mA cm⁻²). As shown in Fig. 3d, FeN₄-700/900 shows the lowest Tafel slope (71 mV dec⁻¹), which is slightly better than commercial Pt/C (72 mV dec⁻¹). This indicates that ORR has the fastest reaction kinetics for FeN₄-700/900 catalysts, further demonstrating the vital effect of the nearby C-O-C structure on improving the ORR performance of Fe-N-C. As electrochemical active surface area (ECSA) is proportional to the electric double layer capacitance (C_{dl}), C_{dl} is calculated from the CV at different sweep speeds to estimate the ECSA (Fig. S17). As shown in Fig. 3e, FeN₄-700/900 shows a larger value of 3.63 mF cm⁻² than those for FeN₄-700/700 (1.84 mF cm⁻²) and FeN₄-900/900 (3.28 mF cm⁻²), revealing its higher effective active area for the ORR. The ORR pathway of Fe-N-C is studied by the rotating ring disk electrode (RRDE) measurements, which show that the H₂O₂ yield of FeN₄-700/900 is below 4% and the corresponding electron transfer number is around 4 (Fig. S16c). According to the slopes of K-L plots, the calculated average electron transfer numbers (n) for FeN₄-700/900 is about 3.9, indicating the preeminent selectivity toward 4e⁻ ORR process (Fig. S18a and S18b), consistent with the findings of the RRDE measurement.

Durability is a further important consideration in evaluating catalyst performance. After 10,000 cycles test, the $E_{1/2}$ of FeN₄-700/900 is negative shifted only 20 mV (Fig. 3f), while Pt/C lost 28 mV. The excellent stability of FeN₄-700/900 is further verified by Chronoamperometric (CA) test (Fig. S16d). After running for 40,000 s, FeN₄-700/900 has 87% of the initial current density, while a 26% reduction is found on commercial Pt/C, informing FeN₄-700/900 exhibits stability for ORR in alkaline electrolyte. Moreover, the methanol tolerance of FeN₄-700/900 is assessed by injecting methanol solution. Compare to commercial Pt/C, FeN₄-700/900 shows excellent methanol tolerance with negligible decay (Fig. S18c). As shown in Fig. S18d, potassium

thiocyanate (KSCN) is used to poison the active site as the SCN⁻ anion has a strong affinity for Fe-N₄. In the presence of KSCN, the current density of FeN₄-700/900 decreased while $E_{1/2}$ negatively shifted over 70 mV, which strongly demonstrates that the atomically dispersed Fe sites contributed to the excellent ORR activity of FeN₄-700/900.

We assemble liquid and flexible all-solid rechargeable Zn-Air Batteries (ZABs) (Fig. 4a) to meet the practical application of Fe-N-C [45]. According to the calculation of the discharge curves (Fig. 4b), FeN₄-700/900 has an excellent peak-power density of 164.4 mW cm⁻² (Fig. 4c) surpassing that of commercial Pt/C (97.1 mW cm⁻²), FeN₄-700/700 (119.8 mW cm⁻²) and FeN₄-900/900 (135.7 mW cm⁻²). The exceptional performance can be attributed to the modulating effect of the C-O-C structure adjacent to Fe-N₄. Furthermore, FeN₄-700/900 can maintain a stable voltage for at least 96 h (1740 cycles) at 2 mA cm⁻², which is significantly superior to the stability of commercial Pt/C, indicating its exceptional long-term stability (Fig. 4d). As shown in Fig. 4e, the performance of the discharge rate is further measured by the discharge voltage at the current density sequence. Specifically, the FeN₄-700/900 cathode shows a small voltage drop at current densities of 2–20 mA cm⁻². When the current density recovered from 20 mA cm⁻² to 2 mA cm⁻², the discharge recovered reversibly, demonstrating the favorable rate performance and stability of the ZAB with FeN₄-700/900. As shown in Fig. S19a, when the current density is 5 mA cm⁻², the specific capacity of FeN₄-700/900 is 695 mAh g_{Zn}⁻¹, which is better than FeN₄-700/700 (650 mAh g_{Zn}⁻¹) and FeN₄-900/900 (569 mAh g_{Zn}⁻¹). Furthermore, FeN₄-700/900 is applied to solid-state ZABs. The all-solid-state batteries display stable charging and discharging potentials at a current density of 2 mA cm⁻² for 2 h, despite the device being bent to 90° and 180° (Figs. S19b and 4f). As shown in Fig. 4g, connecting three solid-state ZABs in series, the voltage can reach 3.2 V, which can light up green (2.0–2.2 V), purple (2.9–3.1 V) and blue (3.0–3.4 V) LED bulbs. All aforementioned results show that FeN₄-700/900 catalysts have a broad practical application prospect.

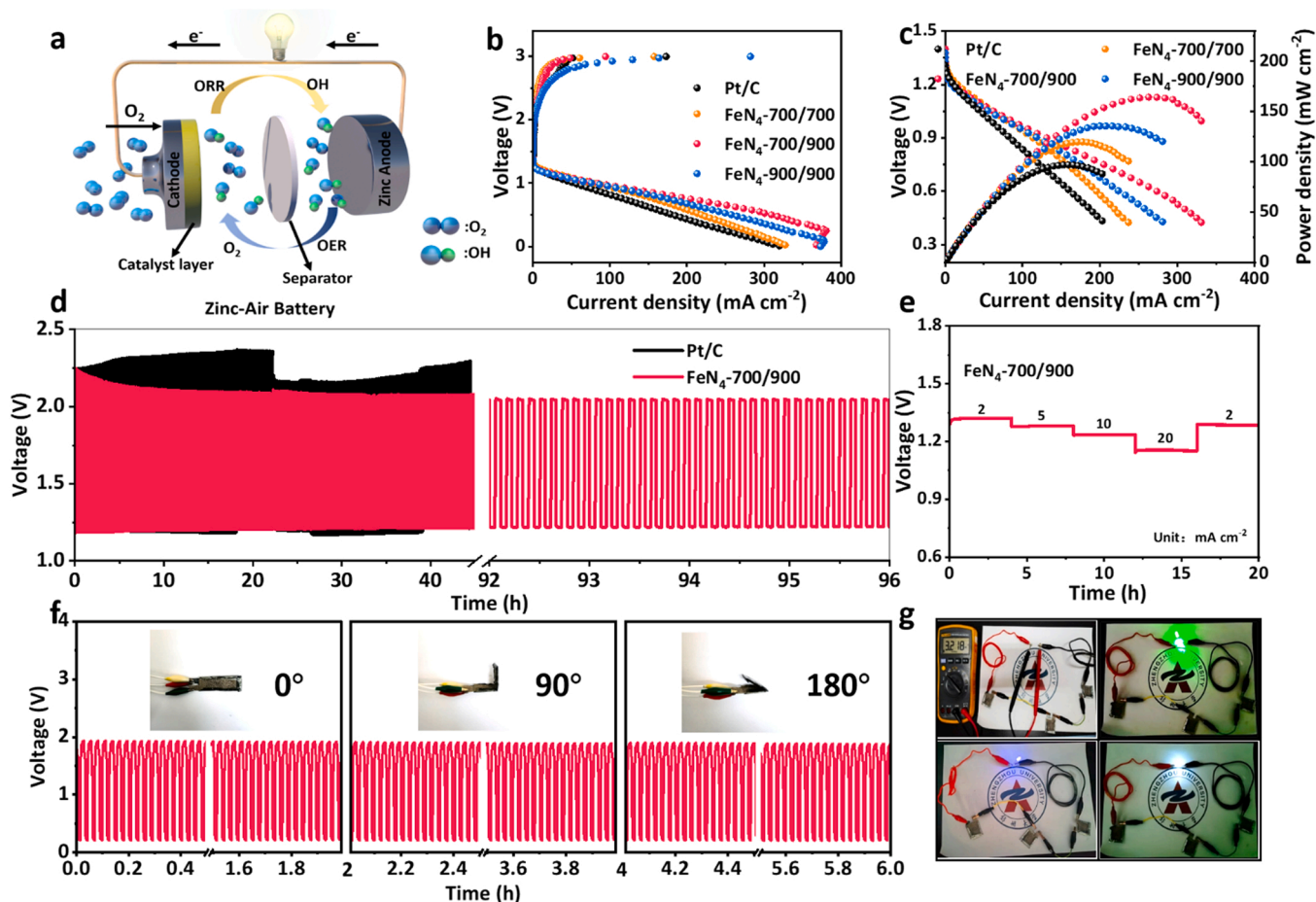


Fig. 4. The performance of Zn-Air Batteries system of Fe-N-C catalysts. (a) Schematic representation of the liquid rechargeable ZAB. (b) Charge and discharge polarization curves of Zn-air batteries. (c) Polarization and power density curves of the primary Zn-air batteries of the FeN₄-700/700, FeN₄-700/900, FeN₄-900/900 catalysts and Pt/C in O₂-saturated 6 M KOH solution. (d) Charge-discharge cycling performance of rechargeable Zn-air batteries at a constant charge-discharge current density of 5 mA cm⁻². (e) Galvanostatic discharge curves of the primary Zn-air battery with FeN₄-700/900 as catalyst at different current densities, which was normalized to the area of air-cathode. (f) Galvanostatic discharge-charge cycling curve at 2 mA cm⁻² for the all-solid-state rechargeable ZAB, applying bending strain (as depicted by the inset images) every 2 h. (g) Photograph of all-solid-state zinc-air battery displaying a measured open-circuit voltage of 3.218 V. Photograph of a lighted LED powered by three all-solid-state Zn-air batteries.

4. Conclusions

In summary, to probe the mechanism of the effect of O-doping on the active center, which is inevitable in the synthesis of Fe-N-C, DFT calculations firstly predict that O-doping promotes the charge separation of the Fe-N₄ active center and weakens the adsorption of oxygenated intermediates. In particular, the C-O-C structure adjacent to FeN₄ significantly reduces the reaction energy barrier and improves the ORR performance. In view of the favorable effect of the C-O-C structure on FeN₄, carbon substrates with different O-doping degrees obtained by treating the chestnut inner shell at different temperatures are used to prepare Fe-single atom catalysts. N, O co-coordinated Fe SACs (FeN₄-700/700), C-O-C activated Fe-N₄ (FeN₄-700/900) and standard Fe-N₄ (FeN₄-900/900) are synthesized as the carbonization temperature is increased. As expected, FeN₄-700/900 catalysts exhibit excellent ORR activity and Zn-air battery performance compared to other comparative samples and Pt/C, strongly confirming the unique advantage of the C-O-C structure adjacent to FeN₄. This work provides new research insights for the practical application of Fe-N-C catalysts.

CRediT authorship contribution statement

Bin Zhao: Conceptualization, Investigation, Methodology, Writing – original draft. **Dongping Xue:** Conceptualization, Investigation,

Methodology, Writing – original draft. **Wenfu Yan:** Writing – review & editing. **Pengfei Yuan:** Theoretical calculation. **Jiangwei Zhang:** Supervision & review. **Shichun Mu:** Project administration, Supervision, Writing – review & editing. **Jianan Zhang:** Conceptualization, Supervision, Writing – review & editing. All authors discussed the results and commented on the article.

Declaration of Competing Interest

The authors declare that they have no known competing financial interests or personal relationships that could have appeared to influence the work reported in this paper.

Data availability

The authors do not have permission to share data.

Acknowledgements

The authors acknowledge the financial support from the National Natural Science Foundation of China (Nos. 21875221, U22A20107), the Youth Talent Support Program of High-Level Talents Special Support Plan in Henan Province (ZYQR201810148), and Creative Talents in the Education Department of Henan Province (19HASTIT039), Academic

Degrees & Graduate Education Reform Project of Henan Province (2021 SJGLX 093Y). We acknowledge the Beijing Synchrotron Radiation Facility (BSRF) 1W1B station for XAS measurements. We also acknowledge the BL11U beamline from the National Synchrotron Radiation Laboratory (NSRL) in Hefei, China, for providing the soft X-ray measurements.

Appendix A. Supporting information

Supplementary data associated with this article can be found in the online version at [doi:10.1016/j.apcatb.2022.122251](https://doi.org/10.1016/j.apcatb.2022.122251).

References

- [1] J. Lai, B. Huang, Y. Tang, F. Lin, P. Zhou, X. Chen, Y. Sun, F. Lv, S. Guo, Barrier-free interface electron transfer on PtFe₂C₂ janus-like nanoparticles boosts oxygen catalysis, *Chem* 4 (2018) 1153–1166, <https://doi.org/10.1016/j.chempr.2018.02.010>.
- [2] H. Huang, D. Yu, F. Hu, S.C. Huang, J. Song, H.Y. Chen, L.L. Li, S. Peng, Clusters induced electron redistribution to tune oxygen reduction activity of transition metal single-atom for metal-air batteries, *Angew. Chem. Int. Ed. Engl.* 61 (2022), e202116068, <https://doi.org/10.1002/anie.202116068>.
- [3] X. Wang, Y. Jia, X. Mao, D. Liu, W. He, J. Li, J. Liu, X. Yan, J. Chen, L. Song, A. Du, X. Yao, Edge-rich Fe-N₄ active sites in defective carbon for oxygen reduction catalysis, *Adv. Mater.* 32 (2020), e2000966, <https://doi.org/10.1002/adma.202000966>.
- [4] L. Zhou, P. Zhou, Y. Zhang, B. Liu, P. Gao, S. Guo, 3D star-like atypical hybrid MOF derived single-atom catalyst boosts oxygen reduction catalysis, *J. Energy Chem.* 55 (2021) 355–360, <https://doi.org/10.1016/j.jechem.2020.06.059>.
- [5] Y. Qiao, P. Yuan, Y. Hu, J. Zhang, S. Mu, J. Zhou, H. Li, H. Xia, J. He, Q. Xu, Sulfuration of an Fe-N-C catalyst containing Fe_xC/Fe species to enhance the catalysis of oxygen reduction in acidic media and for use in flexible Zn-air batteries, *Adv. Mater.* 30 (2018), e1804504, <https://doi.org/10.1002/adma.201804504>.
- [6] P. Zhang, Y. Wang, Y. You, J. Yuan, Z. Zhou, S. Sun, Generation pathway of hydroxyl radical in Fe/N/C-based oxygen reduction electrocatalysts under acidic media, *J. Phys. Chem. Lett.* 12 (2021) 7797–7803, <https://doi.org/10.1021/acs.jpclett.1c01905>.
- [7] J. Yang, Z. Wang, C.X. Huang, Y. Zhang, Q. Zhang, C. Chen, J. Du, X. Zhou, Y. Zhang, H. Zhou, L. Wang, X. Zheng, L. Gu, L.M. Yang, Y. Wu, Compressive strain modulation of single iron sites on helical carbon support boosts electrocatalytic oxygen reduction, *Angew. Chem. Int. Ed. Engl.* 60 (2021) 22722–22728, <https://doi.org/10.1002/anie.202109058>.
- [8] X. Zhang, S. Zhang, Y. Yang, L. Wang, Z. Mu, H. Zhu, X. Zhu, H. Xing, H. Xia, B. Huang, J. Li, S. Guo, E. Wang, A general method for transition metal single atoms anchored on honeycomb-like nitrogen-doped carbon nanosheets, *Adv. Mater.* 32 (2020), e1906905, <https://doi.org/10.1002/adma.201906905>.
- [9] J. Zhu, Y. Huang, W. Mei, C. Zhao, J. Zhang, J.S. Amiin, S. Mu, Effects of intrinsic pentagon defects on electrochemical reactivity of carbon nanomaterials, *Angew. Chem. Int. Ed. Engl.* 58 (2019) 3859–3864, <https://doi.org/10.1002/anie.201813805>.
- [10] C. Zhang, Y.C. Wang, B. An, R. Huang, C. Wang, Z. Zhou, W. Lin, Networking pyrolyzed zeolitic imidazolate frameworks by carbon nanotubes improves conductivity and enhances oxygen-reduction performance in polymer-electrolyte-membrane fuel cells, *Adv. Mater.* 29 (2017), <https://doi.org/10.1002/adma.201604556>.
- [11] Y. Yao, M. Chen, R. Xu, S. Zeng, H. Yang, S. Ye, F. Liu, X. Wu, Y. Yu, CNT interwoven nitrogen and oxygen dual-doped porous carbon nanosheets as free-standing electrodes for high-performance Na-Se and K-Se flexible batteries, *Adv. Mater.* 30 (2018), e1805234, <https://doi.org/10.1002/adma.201805234>.
- [12] J. Guo, B. Li, Q. Zhang, Q. Liu, Z. Wang, Y. Zhao, J. Shui, Z. Xiang, Highly accessible atomically dispersed Fe-N_x sites electrocatalyst for proton-exchange membrane fuel cell, *Adv. Sci.* 8 (2021), 2002249, <https://doi.org/10.1002/adv.202002249>.
- [13] X. Wang, Y. Wang, X. Sang, W. Zheng, S. Zhang, L. Shuai, B. Yang, Z. Li, J. Chen, L. Lei, N.M. Adli, M.K.H. Leung, M. Qiu, G. Wu, Y. Hou, Dynamic activation of adsorbed intermediates via axial traction for the promoted electrochemical CO₂ reduction, *Angew. Chem. Int. Ed. Engl.* 60 (2021) 4192–4198, <https://doi.org/10.1002/anie.202013427>.
- [14] E. Jung, H. Shin, B.H. Lee, V. Efremov, S. Lee, H.S. Lee, J. Kim, W. Hooch Antink, S. Park, K.S. Lee, S.P. Cho, J.S. Yoo, Y.E. Sung, T. Hyeon, Atomic-level tuning of Co-N-C catalyst for high-performance electrochemical H₂O₂ production, *Nat. Mater.* 19 (2020) 436–442, <https://doi.org/10.1038/s41563-019-0571-5>.
- [15] Y. Gu, B.J. Xi, H. Zhang, Y.C. Ma, S.L. Xiong, Activation of main-group antimony atomic sites for oxygen reduction catalysis, e202202200, *Angew. Chem. Int. Ed. Engl.* (2022), <https://doi.org/10.1002/anie.202202200>.
- [16] P. Chen, L.-K. Wang, G. Wang, M.-R. Gao, J. Ge, W.-J. Yuan, Y.-H. Shen, A.-J. Xie, S.-H. Yu, Nitrogen-doped nanoporous carbon nanosheets derived from plant biomass: an efficient catalyst for oxygen reduction reaction, *Energy Environ. Sci.* 7 (2014) 4095–4103, <https://doi.org/10.1039/c4ee02531h>.
- [17] H. Zhao, D. Lu, J. Wang, W. Tu, D. Wu, S.W. Koh, P. Gao, Z.J. Xu, S. Deng, Y. Zhou, B. You, H. Li, Raw biomass electroreforming coupled to green hydrogen generation, *Nat. Commun.* 12 (2021) 2008, <https://doi.org/10.1038/s41467-021-22250-9>.
- [18] J. Wang, Y. Yao, C. Zhang, Q. Sun, D. Cheng, X. Huang, J. Feng, J. Wan, J. Zou, C. Liu, C. Yu, Superstructured macroporous carbon rods composed of defective graphitic nanosheets for efficient oxygen reduction reaction, *Adv. Sci.* 8 (2021), e2100120, <https://doi.org/10.1002/adv.202100120>.
- [19] L. Du, G. Zhang, X. Liu, A. Hassanpour, M. Dubois, A.C. Tavares, S. Sun, Biomass-derived nonprecious metal catalysts for oxygen reduction reaction: the demand-oriented engineering of active sites and structures, *Carbon Energy* 2 (2020) 561–581, <https://doi.org/10.1002/cey2.73>.
- [20] L. Zhong, C. Jiang, M. Zheng, X. Peng, T. Liu, S. Xi, X. Chi, Q. Zhang, L. Gu, S. Zhang, G. Shi, L. Zhang, K. Wu, Z. Chen, T. Li, M. Dahbi, J. Alami, K. Amine, J. Lu, Wood carbon based single-atom catalyst for rechargeable Zn-air batteries, *ACS Energy Lett.* 6 (2021) 3624–3633, <https://doi.org/10.1021/acseenergylett.1c01678>.
- [21] X. Zhang, D. Xue, S. Jiang, H. Xia, Y. Yang, W. Yan, J. Hu, J. Zhang, Rational confinement engineering of MOF-derived carbon-based electrocatalysts toward CO₂ reduction and O₂ reduction reactions, *InfoMat.* 4 (2021), e12257, <https://doi.org/10.1002/inf2.12257>.
- [22] P. Qiu, B. Ma, C.T. Hung, W. Li, D. Zhao, Spherical mesoporous materials from single to multilevel architectures, *Acc. Chem. Res.* 52 (2019) 2928–2938, <https://doi.org/10.1021/acs.accounts.9b00357>.
- [23] H. Yin, P. Yuan, B.-A. Lu, H. Xia, K. Guo, G. Yang, G. Qu, D. Xue, Y. Hu, J. Cheng, S. Mu, J.-N. Zhang, Phosphorus-driven electron delocalization on edge-type FeN₄ active sites for oxygen reduction in acid medium, *ACS Catal.* 11 (2021) 12754–12762, <https://doi.org/10.1021/acscatal.1c02259>.
- [24] B. Ravel, M. Newville, ATHENA, ARTEMIS, HEPHAESTUS: data analysis for X-ray absorption spectroscopy using IFFFIT, *J. Synchrotron Radiat.* 12 (2005) 537–541, <https://doi.org/10.1107/S0909049505012719>.
- [25] R.G. Jones, X-ray absorption: principles, applications, techniques of EXAFS, SEXAFS, and XANES: Edited by D.C. Koningsberger and R. Prins, pp. 673, Wiley, Chichester, 1988. £77.50, Endeavour. 12 (1988), 195, [https://doi.org/https://doi.org/10.1016/0160-9327\(88\)90177-9](https://doi.org/https://doi.org/10.1016/0160-9327(88)90177-9).
- [26] J.J. Rehr, R.C. Albers, Theoretical approaches to x-ray absorption fine structure, *Rev. Mod. Phys.* 72 (2000) 621–654, <https://doi.org/10.1103/RevModPhys.72.621>.
- [27] L. Wang, C. Zhu, M. Xu, C. Zhao, J. Gu, L. Cao, X. Zhang, Z. Sun, S. Wei, W. Zhou, W.X. Li, J. Lu, Boosting activity and stability of metal single-atom catalysts via regulation of coordination number and local composition, *J. Am. Chem. Soc.* 143 (2021) 18854–18858, <https://doi.org/10.1021/jacs.1c09498>.
- [28] A. Ejaz, S. Jeon, The individual role of pyrrolic, pyridinic and graphitic nitrogen in the growth kinetics of Pd NPs on N-rGO followed by a comprehensive study on ORR, *Int. J. Hydrog. Energy* 43 (2018) 5690–5702, <https://doi.org/10.1016/j.ijhydene.2017.12.184>.
- [29] F. Liu, L. Shi, X. Lin, D. Yu, C. Zhang, R. Xu, D. Liu, J. Qiu, L. Dai, Site-density engineering of single-atomic iron catalysts for high-performance proton exchange membrane fuel cells, *Appl. Catal. B.* 302 (2022), <https://doi.org/10.1016/j.apcatb.2021.120860>.
- [30] J. Yang, W. Li, D. Wang, Y. Li, Electronic metal-support interaction of single-atom catalysts and applications in electrocatalysis, *Adv. Mater.* 32 (2020), e2003300, <https://doi.org/10.1002/adma.202003300>.
- [31] J.K. Nørskov, Electronic factors in catalysis, *Prog. Surf. Sci.* 38 (1991) 103–144, [https://doi.org/10.1016/0079-6816\(91\)90007-Q](https://doi.org/10.1016/0079-6816(91)90007-Q).
- [32] G.F. Han, F. Li, W. Zou, M. Karamad, J.P. Jeon, S.W. Kim, S.J. Kim, Y. Bu, Z. Fu, Y. Lu, S. Siahrostami, J.B. Baek, Building and identifying highly active oxygenated groups in carbon materials for oxygen reduction to H₂O₂, *Nat. Commun.* 11 (2020) 2209, <https://doi.org/10.1038/s41467-020-15782-z>.
- [33] J. Gao, Y. Hu, Y. Wang, X. Lin, K. Hu, X. Lin, G. Xie, X. Liu, K.M. Reddy, Q. Yuan, H. J. Qiu, MOF structure engineering to synthesize CoNC catalyst with richer accessible active sites for enhanced oxygen reduction, *Small* 17 (2021), e2104684, <https://doi.org/10.1002/sml.202104684>.
- [34] Y. Chen, S. Ji, Y. Wang, J. Dong, W. Chen, Z. Li, R. Shen, L. Zheng, Z. Zhuang, D. Wang, Y. Li, Isolated single iron atoms anchored on N-doped porous carbon as an efficient electrocatalyst for the oxygen reduction reaction, *Angew. Chem. Int. Ed. Engl.* 56 (2017) 6937–6941, <https://doi.org/10.1002/anie.201702473>.
- [35] H. Zhang, S. Hwang, M. Wang, Z. Feng, S. Karakalos, L. Luo, Z. Qiao, X. Xie, C. Wang, D. Su, Y. Shao, G. Wu, Single atomic iron catalysts for oxygen reduction in acidic media: particle size control and thermal activation, *J. Am. Chem. Soc.* 139 (2017) 14143–14149, <https://doi.org/10.1021/jacs.7b06514>.
- [36] Z. Miao, X. Wang, Z. Zhao, W. Zuo, S. Chen, Z. Li, Y. He, J. Liang, F. Ma, H.L. Wang, G. Lu, Y. Huang, G. Wu, Q. Li, Improving the stability of non-noble-metal M-N-C catalysts for proton-exchange-membrane fuel cells through M-N bond length and coordination regulation, *Adv. Mater.* 33 (2021), e2006613, <https://doi.org/10.1002/adma.202006613>.
- [37] F. Kong, R. Si, N. Chen, Q. Wang, J. Li, G. Yin, M. Gu, J. Wang, L.-M. Liu, X. Sun, Origin of hetero-nuclear Au-Co dual atoms for efficient acidic oxygen reduction, *Appl. Catal. B.* 301 (2022), <https://doi.org/10.1016/j.apcatb.2021.120782>.
- [38] M. Zhao, H. Liu, H. Zhang, W. Chen, H. Sun, Z. Wang, B. Zhang, L. Song, Y. Yang, C. Ma, Y. Han, W. Huang, A. pH-universal, ORR catalyst with single-atom iron sites derived from a double-layer MOF for superior flexible quasi-solid-state rechargeable Zn-air batteries, *Energy Environ. Sci.* 14 (2021) 6455–6463, <https://doi.org/10.1039/d1ee01602d>.
- [39] L. Jiao, J. Li, L.L. Richard, Q. Sun, T. Stracensky, E. Liu, M.T. Sougrati, Z. Zhao, F. Yang, S. Zhong, H. Xu, S. Mukerjee, Y. Huang, D.A. Cullen, J.H. Park, M. Ferrandon, D.J. Myers, F. Jaouen, Q. Jia, Chemical vapour deposition of Fe-N-C

- oxygen reduction catalysts with full utilization of dense Fe-N₄ sites, *Nat. Mater.* 20 (2021) 1385–1391, <https://doi.org/10.1038/s41563-021-01030-2>.
- [40] L. Zong, K. Fan, W. Wu, L. Cui, L. Zhang, B. Johannessen, D. Qi, H. Yin, Y. Wang, P. Liu, L. Wang, H. Zhao, Anchoring single copper atoms to microporous carbon spheres as high-performance electrocatalyst for oxygen reduction reaction, *Adv. Funct. Mater.* 31 (2021), <https://doi.org/10.1002/adfm.202104864>.
- [41] X. Xie, L. Peng, H. Yang, G.I.N. Waterhouse, L. Shang, T. Zhang, MIL-101-derived mesoporous carbon supporting highly exposed Fe single-atom sites as efficient oxygen reduction reaction catalysts, *Adv. Mater.* 33 (2021), e2101038, <https://doi.org/10.1002/adma.202101038>.
- [42] D. Menga, J.L. Low, Y.S. Li, I. Arcon, B. Koyuturk, F. Wagner, F. Ruiz-Zepeda, M. Gaberscek, B. Paulus, T.P. Fellerger, Resolving the dilemma of Fe-N-C catalysts by the selective synthesis of tetrapyrrolic active sites via an imprinting strategy, *J. Am. Chem. Soc.* 143 (2021) 18010–18019, <https://doi.org/10.1021/jacs.1c04884>.
- [43] H. Zhou, T. Yang, Z. Kou, L. Shen, Y. Zhao, Z. Wang, X. Wang, Z. Yang, J. Du, J. Xu, M. Chen, L. Tian, W. Guo, Q. Wang, H. Lv, W. Chen, X. Hong, J. Luo, D. He, Y. Wu, Negative pressure pyrolysis induced highly accessible single sites dispersed on 3D graphene frameworks for enhanced oxygen reduction, *Angew. Chem. Int. Ed. Engl.* 59 (2020) 20465–20469, <https://doi.org/10.1002/anie.202009700>.
- [44] Q. Wang, Y. Yang, F. Sun, G. Chen, J. Wang, L. Peng, W.T. Chen, L. Shang, J. Zhao, D. Sun-Waterhouse, T. Zhang, G.I.N. Waterhouse, Molten NaCl-assisted synthesis of porous Fe-N-C electrocatalysts with a high density of catalytically accessible FeN₄ active sites and outstanding oxygen reduction reaction performance, *Adv. Energy Mater.* 11 (2021), <https://doi.org/10.1002/aenm.202100219>.
- [45] G. Yang, J. Zhu, P. Yuan, Y. Hu, G. Qu, B.A. Lu, X. Xue, H. Yin, W. Cheng, J. Cheng, W. Xu, J. Li, J. Hu, S. Mu, J.N. Zhang, Regulating Fe-spin state by atomically dispersed Mn-N in Fe-N-C catalysts with high oxygen reduction activity, *Nat. Commun.* 12 (2021) 1734, <https://doi.org/10.1038/s41467-021-21919-5>.